J Mater Sci: Mater Med (2011) 22:1393–1406
DOI 10.1007/s10856-011-4321-8

Laser surface modification for synthesis of textured bioactive and biocompatible Ca–P coatings on Ti–6Al–4V

Sameer R. Paital · Nancy Bunce · Peeyush Nandwana · Chinmay Honrao · Soumya Nag · Wei He · Rajarshi Banerjee · Narendra B. Dahotre

Received: 19 January 2011 / Accepted: 7 April 2011 / Published online: 28 April 2011

Abstract A textured calcium phosphate based bio-ceramic coating was synthesized by continuous wave Nd:YAG laser induced direct melting of hydroxyapatite precursor on Ti–6Al–4V substrate. Two different micro-textured patterns (100 μm and 200 μm line spacing) of Ca–P based phases were fabricated by this technique to understand the alignment and focal adhesion of the bone forming cells on these surfaces. X-ray diffraction studies of the coated samples indicated the presence of $CaTiO_3$, α-$Ca_3(PO_4)_2$, $Ca(OH)_2$, TiO_2 (anatase) and TiO_2 (rutile) phases as a result of the intermixing between the precursor and substrate material during laser processing. A two dimensional elemental mapping of the cross-section of the coated samples exhibited the presence of higher phosphorous concentration within the coating and a thin layer of calcium concentration only at the top of the coating. Improved in vitro bioactivity and in vitro biocompatibility was observed for the laser processed samples as compared to the control.

1 Introduction

Biological responses to biomaterials are largely controlled by the surface chemistry and surface morphology. Therefore, surface modification of biomaterials to provide the appropriate biological response without altering the bulk mechanical and functionality of the device is an area of key research [1, 2]. For load bearing implant applications, the most common surface modification approach to improve bonding and bone growth at the interface is to provide a calcium phosphate (Ca–P) based bioceramic coating on Ti–6Al–4V alloys. Here, the Ti–6Al–4V metallic alloy, owing to its superior mechanical properties (tensile strength and fatigue), chemical stability (corrosion resistance), and biocompatibility under in vivo conditions maintain the bulk mechanical and functionality of the implant device. On the other hand, the hydroxyapatite (HA, $Ca_{10}(PO_4)_6(OH)_2$) based Ca–P ceramics mimic the naturally occurring bone mineral in terms of their chemical composition and crystallographic structure and hence is considered as a coating material on Ti–6Al–4V for direct bone bonding by attachment, proliferation and differentiation of bone forming cells.

The various methods that have been carried out to develop Ca–P coatings on Ti alloys include plasma spray deposition [3], magnetron sputtering [4], sol–gel-based

---

S. R. Paital · P. Nandwana · S. Nag · R. Banerjee ·
N. B. Dahotre (✉)
Department of Materials Science and Engineering,
University of North Texas, Denton, TX 76207, USA
e-mail: Narendra.Dahotre@unt.edu

N. Bunce
Center for Advanced Research and Technology,
University of North Texas, Denton, TX 76207, USA

C. Honrao
Metallurgical and Materials Engineering, Indian Institute
of Technology Kharagpur, Kharagpur 721302, India

W. He
Department of Materials Science and Engineering,
The University of Tennessee, Knoxville, TN 37996, USA

W. He
Department of Mechanical, Aerospace and Biomedical
Engineering, The University of Tennessee, Knoxville,
TN 37996, USA

coatings [5], pulsed laser deposition [6], electrophoretic deposition [7]. Although, most of these coating techniques are aimed to enhance short and long-term performance of implants by encouraging bone in-growth and providing enhanced fixation, they fail to achieve both a controlled or regular topographic cue (surface physical texture) and improved bonding at the substrate and coating interface simultaneously. The presence of a weak bonding between the coating and substrate material often results in the disintegration and delamination of the coating after prolonged use. The debris generated due to such failure stimulates inflammation and thereby eventually results in loosening of the prosthetic device [8–10]. The topographic cues in the form of grooves, porosity, roughness and surface physical texture provide contact guidance and adhesion of the bone forming cells at the tissue implant interface [11]. It is hypothesized that these three dimensional irregularities at the implant surface provide a local difference in surface free energy and result in a specific deposition pattern of the substratum bound attachment proteins [11]. This spatial arrangement of attached proteins affects the wettability of the implant material and thereby the attachment and orientation of the bone forming cells. However, for most of the above mentioned coating techniques, the surface topographic cues are of random nature and there is no control on their length scales. Because of these associated drawbacks there has been significant research in terms of modifying the surface of an implant material to synthesize controlled and regular topographic cues with improved bonding between the coating and the substrate material.

In our group we proposed a laser based surface modification approach to synthesize simultaneously a topographically textured and bioactive Ca–P coating on Ti–6Al–4V [12–16]. The laser based surface modification approach to provide improved bioactive and biocompatible coatings has been well established by many previous excellent works [17–22]. Hence, in this current effort we used such a technique where a continuous wave (CW) Nd:YAG laser source was employed to synthesize the textured Ca–P coatings. The highly intense laser beam from the CW Nd:YAG laser was used to melt both the precursor (HA) and substrate (Ti–6Al–4V) and thereby provide a metallurgical bonding at the interface. Further, as the laser scanning process can be programmed to achieve line patterns at varying lateral track spacings (center to center distance between laser tracks), micro-textured patterns at varying length scales can also be obtained by this technique. The effect of laser processing parameters on the evolution of the micro-textures, phases and microstructure and thereby its subsequent effect on in vitro bioactivity and in vitro biocompatibility of the coatings is studied.

2 Materials and methods

2.1 Sample preparation and Ca–P coating using a CW laser

The substrate Ti–6Al–4V plates of dimensions 100 × 50 × 3 mm^3 were cut from the rolled sheets using an abrasive cutter. The plates were then polished using a 600 grit silicon carbide emery paper followed by ultrasonic rinsing with acetone to remove any dust and grease. The commercially available HA ($Ca_{10}(PO_4)_6(OH)_2$) powder obtained from Fisher Scientific was taken as the precursor material. The powders had a spherical morphology with a unimodal distribution in the range of 10–30 μm in diameter. X-ray diffraction (XRD) studies conducted on these powders proved for their highly crystalline nature and can be referred from our previously published work [14]. The precursor powder was mixed with a water-based organic solvent LISI W 15853 obtained from Warren Paint and Color Company (Nashville, TN, USA). The mixed slurry was then sprayed onto the preheated (~50°C) substrate coupons using an air-pressurized spray gun. The sprayed coupons were air dried to remove the moisture and a uniform thickness of approximately 80 μm was maintained for all precoating deposits. The coating thickness was measured by scratching of the preplaced precursor at one corner and measuring the change in depth of focus using an optical microscope. Finally, the samples were scanned using a CW Nd:YAG laser equipped with a fiber optic beam delivery system to obtain a textured coating at the surface and a metallurgical bonding at the substrate-coating interface. The fiber optic was interfaced with an end effector that houses a set of spherical and cylindrical lenses to shape the output of the laser beam. The laser was operated in the infrared region with a wavelength of 1064 nm. This infrared laser beam had a Gaussian intensity distribution and was focused on the surface of the sample using a 120 mm focal length convex lens. The laser processing parameters used for the coating process are illustrated in Table 1. It can be observed (Table 1) that in the

Table 1 Laser parameters used in the study

Stand of distance	356 mm from the surface of the sample
Laser spot shape	Circular
Laser spot diameter	400 μm
Laser scan speed	500 mm s^{-1}
Average output power	215 W
Laser fluence or energy density of the laser beam	137 J cm^{-2}
Lateral track spacings	100 and 200 μm

current work only the lateral track spacings are varied keeping the rest of the parameters constant. A lateral track spacings of 100 and 200 μm are chosen so as to match the length scale of the naturally occurring three dimensional extra cellular matrix (ECM) present in the human bone [23]. Contrary to the above, in conventional pre-pasted laser cladding technique the lateral track spacing or the laser spot overlap is decided in such a way that there is controlled re-melting and also minimum dilution caused due to overheating.

2.2 Surface characterization of the Ca–P coatings

The surface microstructures of the textured-coated specimens were studied using a LEO 1525 scanning electron microscope (SEM). The cross-sectional microscopic and compositional analysis of the coatings were studied using a FEI NOVA Nano SEM 230 microscope equipped with a field emission gun (FEG) source, an electron backscatter EBSD detector and an EDS detector. The compositional lines as well as maps were collected using the attached EDS detector and analyzed via the EDAX Genesis Software. The surface roughness of the untreated Ti–6Al–4V and textured coated samples were studied using a Leica optical profilometer, by scanning the laser beam across a surface area of 1500 × 1500 μm^2. The roughness values were recorded in the form of R_a (defined as the arithmetic average of all points of the profile also called the center line average height), R_z (arithmetic average of vertical distances between the highest peak and deepest valley within a sampling length) and R_{max} (maximum individual roughness depth). A total of five random scans each were carried out on both the processing direction and perpendicular to the processing direction of the textured coated samples to get an average within these roughness values.

The phase analyses of the textured coatings were studied using an X-ray diffractometer. A Philips Norelco X-ray diffraction (XRD) system with Cu-$K\alpha$ radiation of wavelength 1.5418 Å was used to study the phase evolution. The XRD system was operated at 20 kV and 10 mA in a 2θ range of 20–100° using a step size of 0.02° and count time of 1 s. The XRD patterns were corrected from any background using the Jade software and the phases were identified by comparing the XRD pattern to ICDD (International center for diffraction data) files obtained from joint committee of powder diffraction standards (JCPDS).

2.3 In vitro bioactivity

The bioactivity or the bio-mineralization behavior of the laser processed samples is studied by soaking the samples in a simulated body fluid (SBF). The SBF solution was prepared by dissolving reagent grade chemicals in the following order: NaCl (8.026 g), $NaHCO_3$ (0.352 g), KCl (0.225 g), $K_2HPO_4 \cdot 3H_2O$ (0.230 g), $MgCl_2 \cdot 6H_2O$(0.311 g), $CaCl_2$ (0.293 g) and Na_2SO_4 (0.072 g) into distilled water (700 ml) and buffering to pH = 7.4 at 37°C by adding tri-hydroxymethylaminomethane (6.063 g) and hydrochloric acid (40 ml) [24, 25]. A 50 ml by volume of the SBF solution was taken in a plastic container and a set of four samples from each processing conditions were completely immersed in the solution. The solution was refreshed every 24 h to maintain a pH of 7.4, and the temperature was maintained at 37°C during the course of the test. The samples were removed from the SBF solution at specified time intervals (1, 3, 5 and 7 days) followed by rinsing with distilled water and air drying for further analysis. A LEO 1525 scanning electron microscope (SEM) was used to observe the microstructure and morphological evolution of the mineralized samples.

The elemental analyses of the mineralized samples were studied using X-ray photoelectron spectroscopy (XPS) techniques. A VersaProbe™ 5000 Scanning XPS Microprobe instrument was used here for the surface elemental analysis of the mineralized layers. Here a monochromatic X-ray beam source at 1486.6 eV and 49.3 W was used to scan upon the sample surface. A high flux X-ray source with Aluminum anode was used for X-ray generation, and a quartz crystal monochromator was used to focus and scan the X-ray beam on the sample. The X-ray beam diameter used was 200 μm and the sample was sputter cleaned and operated at a vacuum pressure of 5×10^{-6} Pascal for the study. The samples used for XPS studies were cleaned with distill water and dried in a vacuum desiccator prior to analysis.

The phase evolution of the mineralized samples was studied using both XRD and Fourier transform infrared (FTIR) spectroscopic techniques. The XRD instrument used here was the same as discussed before for phase analysis of the coatings. The FTIR analysis was carried using a Nicolet FTIR Continuum Infrared Microscope, configured for operation under reflectance and transmission mode. In the current study the solid samples were analyzed under the reflectance mode and the samples were placed on an aluminum coated slide for the background. The spectra were obtained at 4.00 cm^{-1} resolution averaging 100 sample scans and 32 background scans. The acquisition range used was 650–4000 cm^{-1}. The size of the infrared beam that was focused using a reflex aperture was 25 × 25 μm^2.

2.4 In vitro biocompatibility

In vitro biocompatibility of coated samples was evaluated through cell morphology during cell culture studies using the mouse pre-osteoblast MC3T3-E1 (subclone 14) cell line, obtained from American Type Cell Culture Collection (ATCC, Manassas, VA, USA). The cells were maintained in a tissue culture flask using the ATCC recommended cell culture medium at 37°C under 5% CO_2 and 95% air in a humidified incubator. The culture medium was replaced every 3 days and confluent cells were trypsinized and replated (0.25% trypsin–EDTA, Invitrogen, USA) to maintain the cell line.

The coated samples and the control (untreated Ti–6Al–4V) of size 4×4 mm^2 were cleaned with 70% ethanol and then UV sterilized prior to cell culture. The pre-osteoblast cells were then seeded on the surfaces of UV sterilized samples placed in 24-well culture plates at a density of 1×10^4 cells cm^{-2} and stored in the CO_2 incubator (maintained at 37°C under 5% CO_2 and 95% air in a humidified incubator) for 1 day. For cell morphology analysis using SEM, cells cultured on the samples were fixed with 3% glutaraldehyde in 0.1 M cacodylate for 1 h and rinsed three times with phosphate buffered saline (PBS). The samples were further processed in 2% osmium tetroxide in 0.1 M cacodylate for 1 h, dehydrated with a series of increasing concentration of ethanol (25, 50, 70, 95 and 100%), critical point dried and sputter-coated with gold for SEM observation. For immunocytochemical staining of the actin filament, the cells cultured on the samples were fixed with 4% paraformaldehyde (Sigma–Aldrich, USA) in 1 × PBS for 30 min at 4°C. After washing with PBS, the samples were permeabilized with 0.1% Triton X-100 (Fisher Scientific, USA) in 1 × PBS for 5 min, blocked with 1% bovine serum albumin (BSA, Sigma–Aldrich, USA) for 30 min and stained with 2% Alexa 594 conjugated Phalloidin (Invitrogen, USA) fluorescent dye for 1 h. Cell nuclei were counterstained with 0.1% 4′,6-diamidino-2-phenylindole (DAPI, Chemicon, USA) in 1 × PBS for 5 min. Samples were washed three times with 0.05% Tween-20 (Sigma) in 1 × PBS before and after the staining steps. All the staining procedures were carried out at room temperature. High-resolution fluorescence images were captured using an upright fluorescence microscope (Nikon).

3 Results and discussions

Low magnification SEM images (Fig. 1) of the surfaces of the samples clearly show the effect of laser track overlap on the surface morphology of the coatings. It can be observed that by varying the track overlap in the lateral direction, there is controlled re-melting of the previously melted surface and hence surface textures at different length scales (100–200 μm line spacings) can be obtained. The higher magnification SEM images of the corresponding surfaces are included as inset and clearly demonstrate the porous and rough nature of the textured coatings. These micron scale features in the form of porosity or pits are expected to influence the protein interactions under in vivo conditions [23, 26, 27]. The quantitative variation in surface roughness as a result of the varying laser fluence and lateral track spacing was evaluated and compared to the results obtained on untreated Ti–6Al–4V sample. The sample processed with 100 μm line spacing had a R_a, R_z and R_{max} values of 2.5, 20.63 and 28.36 μm respectively and the sample processed with 200 μm line spacing had a R_a, R_z and R_{max} values of 6.5, 53.1 and 71.7 μm respectively. In contrast for the untreated Ti–6Al–4V sample the R_a, R_z and R_{max} values were 2.04, 7.6 and 13.4 μm respectively. Hence, it can be clearly observed that there is a significant increase in surface roughness as a result of laser surface modification. However, within the laser processed samples, it can be observed that the samples processed for 100 μm line spacing have significantly lower values of R_a, R_z and R_{max} as compared to the samples processed for 200 μm line spacing. With reduced lateral track overlap or line spacing, there is an increase in the spot overlap (spot diameter = 400 μm) in the lateral direction

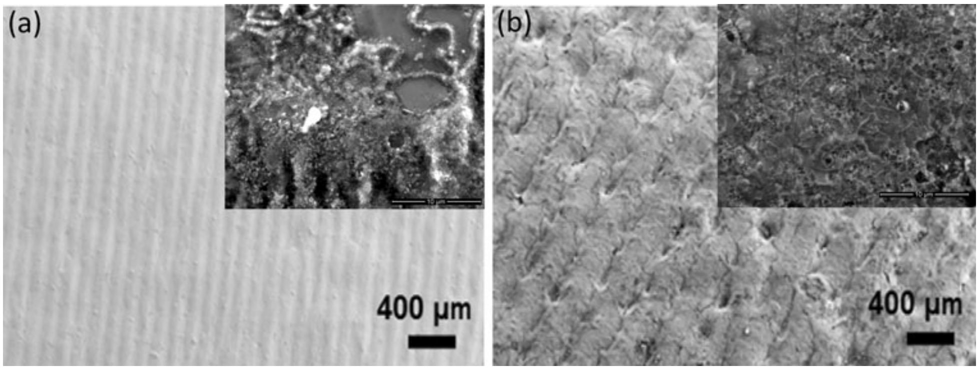

Fig. 1 Low magnification SEM images and its corresponding higher magnification as *inset* for the samples processed at: **a** 137 J cm^{-2}, 100 μm line spacing and **b** 137 J cm^{-2}, 200 μm line spacing

Fig. 2 XRD pattern for the laser processed samples

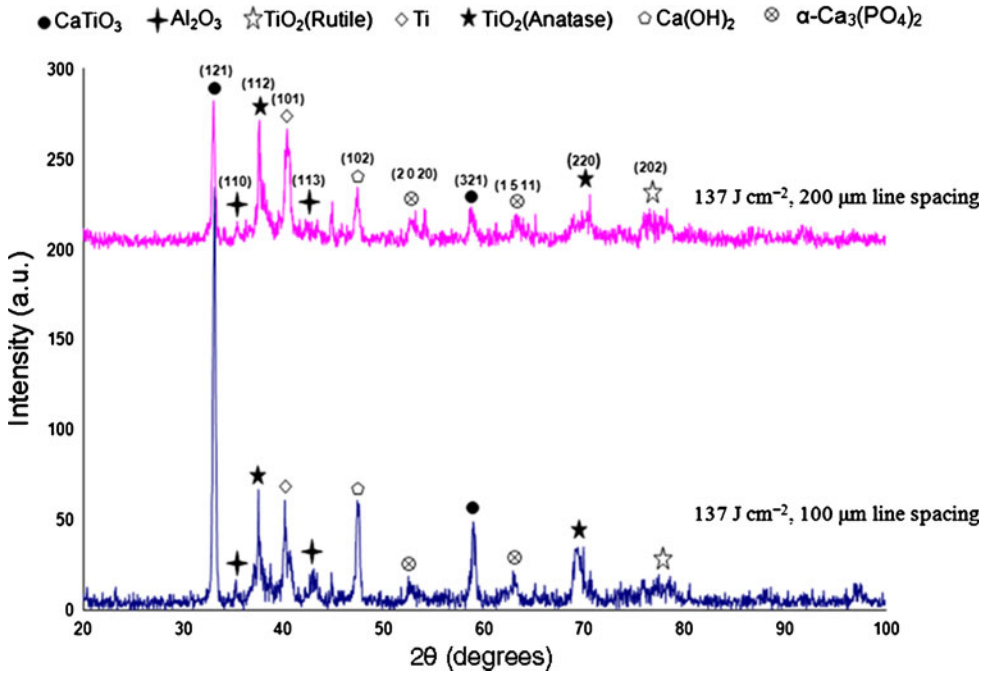

leading to remelting of a predominant amount of the already melted surface. This increased remelting of the ceramic layer because of reduced track overlap is expected to smoothen the surface of the coating. Therefore, laser surface modification demonstrated the potential to synthesize 3-dimensional surface textures at the cellular and supracellular length scales and hence expected to influence the cell-fate process through cell–cell interaction and integration of the implant with the host [11]. XRD results collected from the surfaces of the samples (Fig. 2) indicate that there is no major change in the types of phases with varying lateral track overlap, and $CaTiO_3$, α-$Ca_3(PO_4)_2$ (α-TCP), $Ca(OH)_2$, TiO_2 (Anatase), TiO_2 (Rutile) and Ti are the major phases present within the coatings. Further, as the processing was carried out in an ambient atmosphere with argon as the cover gas, a small amount of oxidation of the melt pool constituents is expected to take place leading to the precipitation of Al_2O_3 at the surface (Fig. 2). Also, as the laser processing is associated with extremely high cooling rates ($\geq 10^{3}$°C S^{-1}), some metastable or amorphous phases were also observed between $2\theta = 30°$ and $2\theta = 45°$.

The effect of laser track overlap on the morphology and composition of the coatings across the cross-section are studied using SEM EDAX 2-D elemental mapping technique. The sample processed at 100 μm line spacing (Fig. 3a) demonstrated a smoother morphology as compared to the sample processed at 200 μm line spacing (Fig. 4a). With reduced lateral track overlap or line spacing, there is an increase in the spot overlap (spot diameter ~400 μm) in the lateral direction, leading to remelting of the already melted surface and thereby smoothening of the coating. The high temperature evolution during laser processing also leads to partial loss of the precursor material due to vaporization and dilution of the coating through intermixing of the elements. The low magnification SEM images and corresponding EDS data as published in one of our previous work suggested for the uniformity of the coating in terms of its composition and surface morphology [28]. Figures 3b–f and 4b–f show the cross-sectional elemental mapping of the sample processed at 100 and 200 μm lateral spacing respectively. It can be observed that only a thin layer of Ca existed at the surface (Figs. 3e, 4e) whereas there is complete penetration of P (Figs. 3f, 4f) within the coating following laser processing. Further their compositional line scans across the cross-section (Figs. 3g, 4g) indicated that Ca exists up to ~10 μm in depth from the surface of the sample, P on the other hand has significantly more penetration depth (~100 μm) most probably due to short circuit interstitial diffusion occurring primarily at α/β interfaces in the Ti–6Al–4V substrate. Such a diffusion pathway, if operational, would not be feasible for a substitutional atom like Ca. However further studies need to be conducted to confirm such a theory. From the above results it can be proved that there is retainment of Ca and P at the surface of the coatings following laser processing. Further, from the XRD studies (Fig. 2) it can be concluded that both Ca and P exist as $CaTiO_3$, $Ca(OH)_2$, and α-TCP phase at the surface of the sample.

Fig. 3 SEM-EDS: **a** cross-section, **b**–**f** cross-section elemental analysis and **g** compositional line scans for Ca and P concentration of the sample processed at 137 J cm^{-2}, 100 µm line spacing

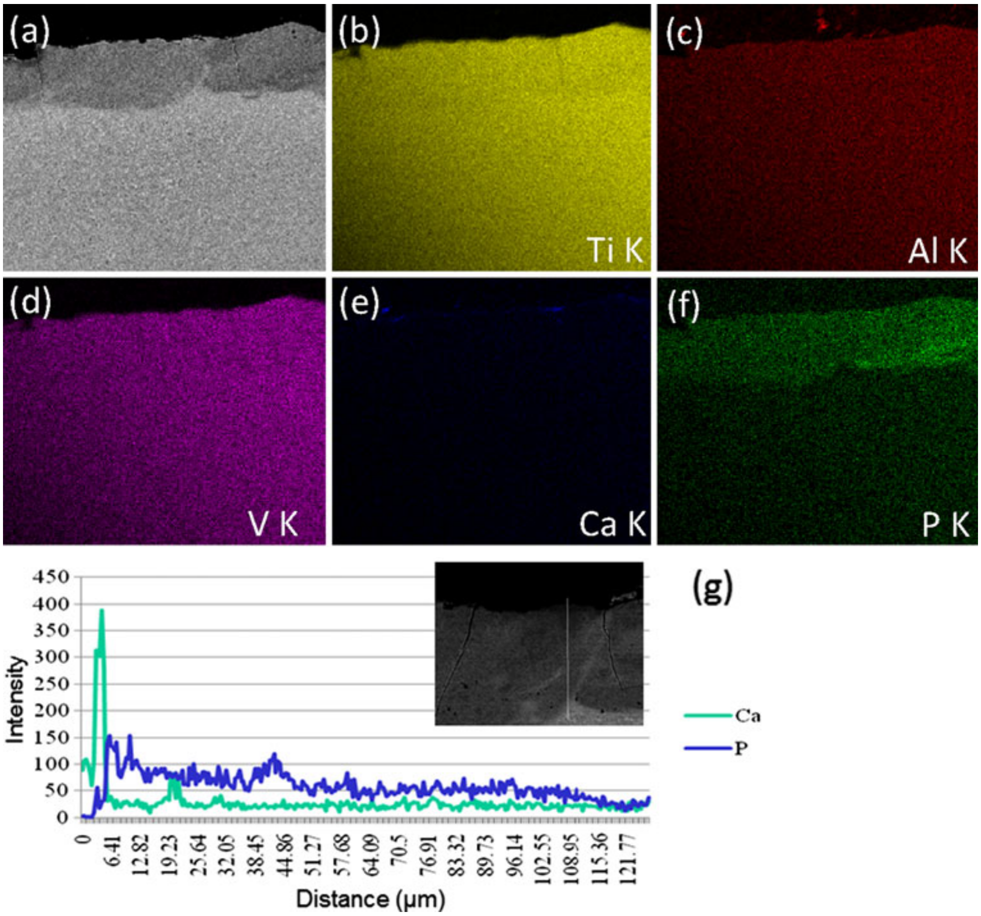

With the retainment of bioactive phases like $CaTiO_3$, $Ca(OH)_2$ and α-TCP, the coated samples were further studied for their in vitro bioactivity or bone bonding ability by immersing in a SBF and analyzing for the precipitation of an apatite (HA) like mineral layer. The precipitation of such a phase on the surface of an implant material under in vivo conditions is beneficial, as HA is a naturally occurring mineral component lying alongside the collagen fibrils. This layer therefore acts as a bone bonding interface, where the cells can preferentially proliferate and differentiate into higher ordered structures such as bone. The presence of an apatite like layer on the untreated samples following immersion in SBF was very minimal as compared to the coatings. Hence the results pertaining to it is not included in the present study. SEM analysis of the coatings following immersion in SBF for 4 different time periods is shown in Fig. 5. It can be observed that irrespective of the laser processing conditions (100 and 200 µm line spacing) change in phase evolution of the coatings with SBF immersion time is the same up to 3 days. Following 1 day immersion in SBF, characteristic whisker-like apatite crystallites are nucleated on both the surfaces of the samples. With the increase in immersion time to 3 days, the whisker-like apatite crystallites transformed into a mixed layer of whisker-like and nano apatite crystals. However, as the immersion time is increased to 5 days the samples processed at 100 µm line spacing got completely covered with nano apatite like phase and after 7 days of immersion period a thick apatite like layer existed on the surface of the sample. In contrast, for the sample processed at 200 µm line spacing, a thick layer of Ca–P phase, uncharacteristic of the HA morphology existed soon after 5 and 7 days of SBF immersion. This improvement in mineralization or bioactivity for the 100 µm line spaced samples might be attributed to its increased hydrophilicity and thereby higher surface energy as calculated in our previous studies [28].

XPS analysis was carried out on the mineralized samples to quantify the elements present on the surface of the samples following immersion in SBF. It can be observed (Fig. 6a, b) that with increasing SBF immersion times there is an increase in the Ca2s, Ca2p, P2s and P2p peaks for both (100 and 200 µm line spacing) laser textured samples. This further confirms the precipitation and improved

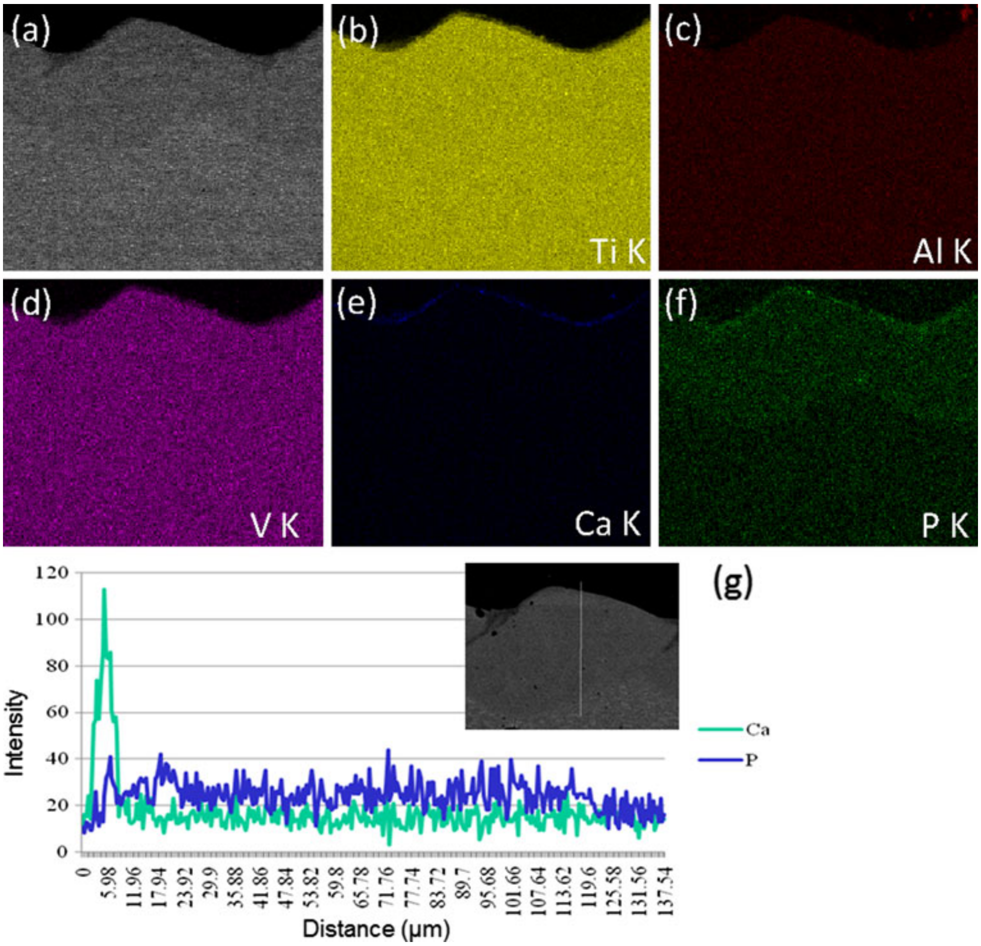

Fig. 4 SEM-EDS: **a** cross-section, **b**–**f** cross-section elemental analysis and **g** compositional line scans for Ca and P concentration of the sample processed at 137 J cm^{-2}, 200 μm line spacing

mineralization of a Ca–P phase under in vitro conditions. To understand the composition of the Ca–P phase, semi-quantitative Ca and P atomic concentration and its ratio (Ca/P) was measured using the integration of peak areas and tabulated in Table 2. It can be observed that for the sample processed at 100 μm line spacing, the Ca\P atomic ratio was in the range of 1.5–1.6 with increasing SBF immersion time, and hence is very close to the Ca\P atomic ratio of stoichiometric HA. In contrast, for the sample processed at 200 μm line spacing, the Ca\P atomic ratio dropped to 1.54 after 1 day SBF immersion and then gradually reduced to ~1.4 with increasing SBF immersion time.

From the XRD studies (Fig. 7a, b), it can be realized that soon after 24 h of SBF immersion a highly intense peak attributable to the HA phase (at 2θ ~31.75 and corresponding to the plane (2 1 1)) was evident for both 100 and 200 μm line spaced sample. As the immersion time is increased to 168 h there is a reduction in intensity along the (2 1 1) plane and a new peak attributable to the HA phase (at 2θ ~21.44 and corresponding to the plane (2 0 0)) showed up for the 100 μm line spaced sample (Fig. 7a). This increased intensity at 2θ ~21.44 and corresponding to the plane (2 0 0) was not evident with increasing SBF immersion time for the 200 μm line spaced sample (Fig. 7b). Further from XRD peaks it is realized that the $CaTiO_3$ peaks (at 2θ ~33.08 and 58.8) reduced in intensity with increasing SBF immersion time for 100 μm line spaced sample (Fig. 7a). In contrast, such a reduction in intensity of the $CaTiO_3$ peaks was not observed for the 200 μm line spaced sample (Fig. 7b). This above phenomenon of the dissolution of $CaTiO_3$ phase and thereby its subsequent precipitation to HA following immersion in SBF can be explained based on the several studies conducted by researchers on the hydrolysis capabilities of $CaTiO_3$ [29, 30]. It has been well demonstrated that the $CaTiO_3$ phase following immersion in SBF undergoes hydrolysis and produces numerous negatively charged OH^- groups on the surface of the implant material as per the following equation [29, 30].

$$CaTiO_{3(s)} + H_2O \rightarrow Ca^{2+} + TiO_{2(s)} + 2OH^-_{(aq)}$$

Fig. 5 SEM surface morphologies of the laser processed samples following immersion in SBF

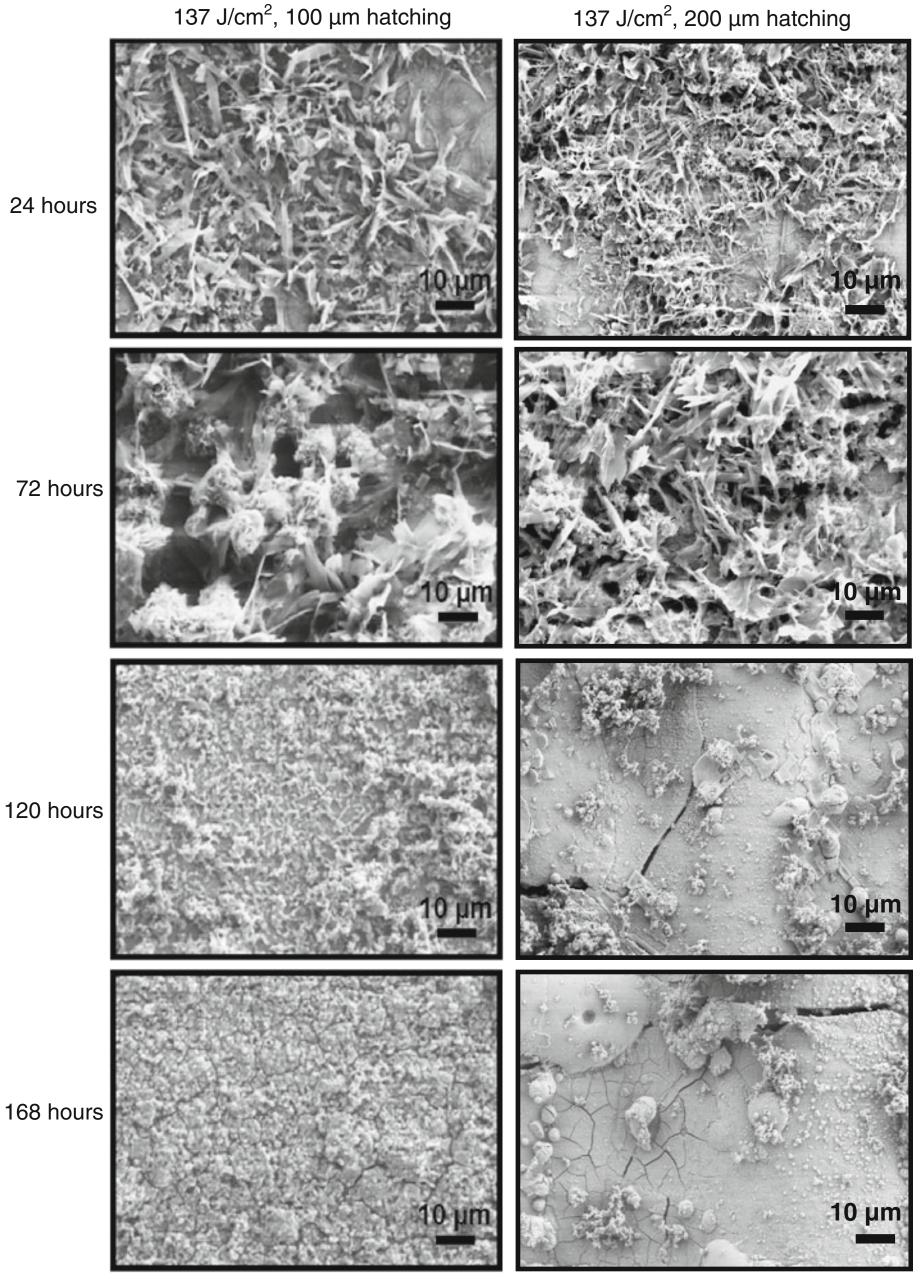

The negatively charged OH^- groups then stimulate the precipitation of calcium ions (Ca^{2+}), and then absorb phosphate ($PO_4{}^{3-}$) and hydrogen carbonate ($HCO_3{}^{2-}$) ions in the SBF due to electrostatic potential interaction. These absorbed calcium and phosphate ions further increase the degree of super saturation of solution with respect to apatite near the surface of an implant material and hence trigger the nucleation of apatite. The preferential attachment and the change in crystallite orientation of the apatite crystals can also be attributed to the strong crystallographic match between $CaTiO_3$ and HA on specific crystal planes [29]. However, such a dissolution of the $CaTiO_3$ phase and preferential attachment of apatite crystals might not have effectively occurred with 200 µm line spaced samples owing to its reduced wettability to SBF [28]. The above results therefore further complement the semi-quantitative XPS (Table 2) data and indicate the presence of a calcium deficient apatite like phase with increasing SBF immersion time for the 200 µm line spaced sample.

The precipitated phase observed using the SEM (Fig. 5), XPS (Fig. 6) and XRD (Fig. 7) studies was further confirmed using the FTIR analysis. The FTIR absorbance

Fig. 6 XPS spectra of laser processed samples: **a** 137 J cm^{-2}, 100 μm line spacing and **b** 137 J cm^{-2}, 200 μm line spacing and following immersion in SBF for different time periods

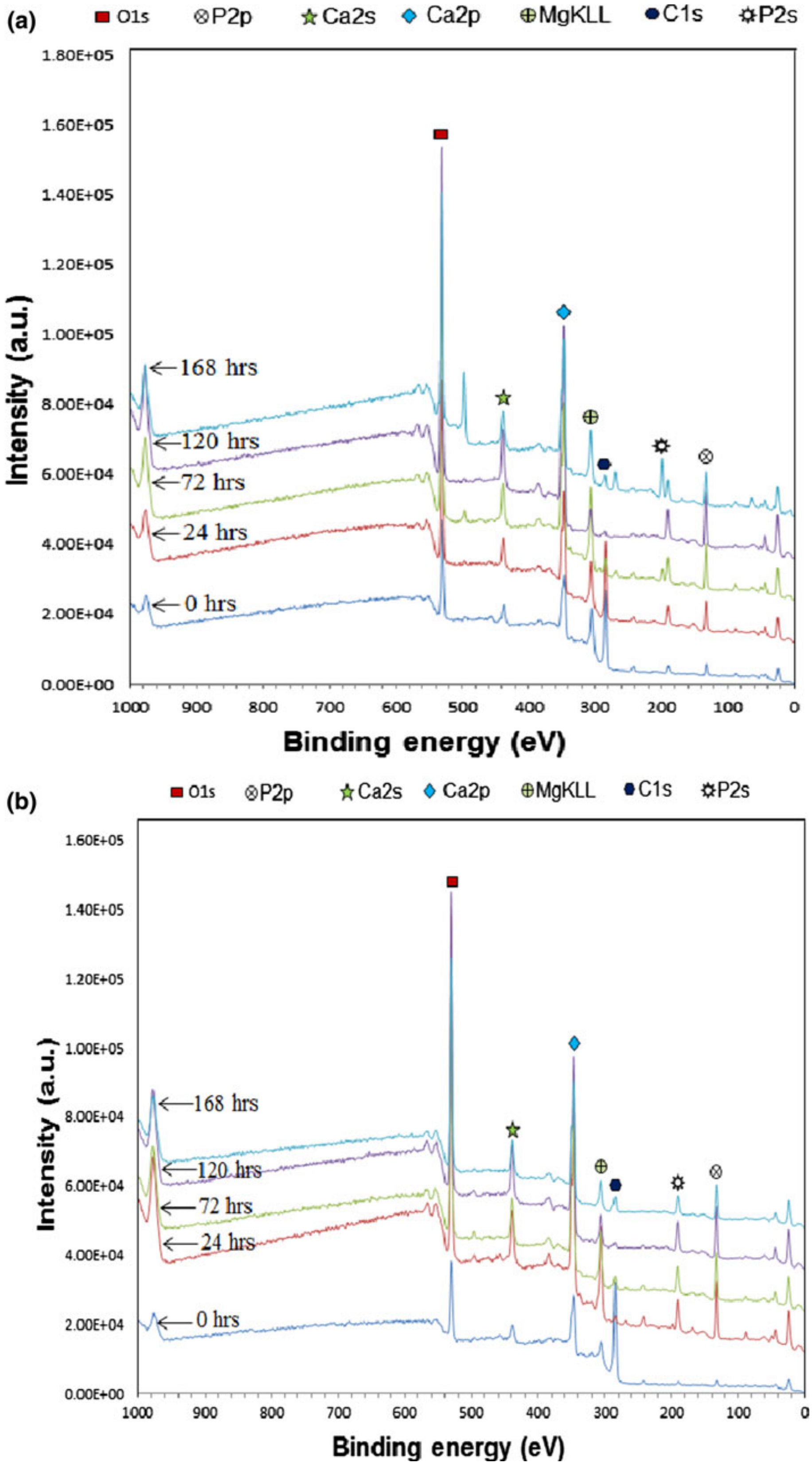

Table 2 Elemental composition and semi-quantitative analysis of Ca and P in terms of atomic concentration for the CW laser processed samples

Sample	SBF immersion time (h)	Elements present	Ca atomic concentration (%)	P atomic concentration (%)	Ca/P atomic ratio
137 J/cm^2, 100 μm line spacing	0	O, C, Ca, P	8.7	3.9	2.23
	24	O, C, Ca, P, Mg	10.2	6.7	1.52
	72	O, C, Ca, P, Mg	15.3	10.0	1.53
	120	O, C, Ca, P, Mg	18.0	11.0	1.63
	168	O, C, Ca, P, Mg	15.3	10.0	1.53
137 J/cm^2, 200 μm line spacing	0	O, C, Ca, P	7.7	2	3.85
	24	O, C, Ca, P, Mg	16.9	11.0	1.54
	72	O, C, Ca, P, Mg	16.6	12.0	1.4
	120	O, C, Ca, P, Mg	17.5	12.4	1.41
	168	O, C, Ca, P, Mg	15.0	10.2	1.47

spectra of the laser textured samples following immersion in SBF for different time periods are presented in Fig. 8. In the spectra, the band at ~3400 cm^{-1} corresponds to the vibration of the hydroxyl ion (OH$^-$) [30, 31]. The band at 667 cm^{-1} is the characteristic band of the phosphate bending vibration, while the band at 990 cm^{-1} is attributed to the phosphate stretching vibration. The band at 1630 cm^{-1} is indicative of the carbonate ion substitution. The analysis of the above bands further confirmed that the spectra shown belong to an apatite like phase. Further with increased SBF immersion time, it can be observed that the phosphate band around 990 cm^{-1} demonstrated an increased intensity. This further confirmed for the increased mineralization behavior of the textured coatings with immersion times. As discussed in our previous work [28], this improvement in mineralization for the textured coatings as compared to the untreated Ti–6Al–4V samples can be attributed to the improvement in wetting behavior or hydrophilicity of the samples following laser surface modification.

The textured coated samples are tested for their in vitro biocompatibility by the culture of mouse MC3T3-E1 osteoblast-like cells and characterizing for cell spreading, morphology and cytoskeleton organization. Based on these findings, an understanding is drawn on the effect of line spacing and appropriate phases on biocompatibility of the coatings. Cell morphology for the laser processed and control (untreated Ti–6Al–4V) samples after 1 day culture of MC3T3-E1 osteoblast-like cells was assessed by SEM and the results are presented in Fig. 9. The MC3T3-E1 osteoblast-like cells show a triangular morphology (Fig. 9a) on the control (untreated Ti–6Al–4V) samples and have a rectangular and elongated morphology on the laser processed samples (Fig. 9b, c). Their sound adhesion especially on the laser processed samples is characterized by the lamellipodia trying to extend and adhere along the grooves. In contrast, no such adhesion is observed on the control (untreated Ti–6Al–4V) sample. Also from the SEM images (Fig. 9) it can be observed that the number of cells on the control (untreated Ti–6Al–4V) sample is significantly less compared to the laser processed samples. Such a difference in cell spreading and adherence on these samples is attributed to both the varying surface chemistry and surface roughness as a result of laser processing. Further, the laser processed samples also provided the appropriate surface morphologies (micro textured surface patterns with 100 and 200 μm line spacing) for the cells to interact and spread on these surfaces.

The fibril networks and spreading of the MC3T3-E1 osteoblast-like cells on the laser textured samples and control (untreated Ti–6Al–4V) are studied from its cytoskeleton organization. The cytoskeletal organization of the cells on the control (untreated Ti–6Al–4V) and laser processed samples after 1 day culture are presented in Fig. 10. The cells appeared to be more confluent with well stressed actin filaments on the laser processed samples as compared to the control (untreated Ti–6Al–4V). This significant improvement in in vitro biocompatibility can therefore be attributed to the improvement in wettability [28] and the presence of appropriate surface morphology and surface chemistry following laser surface modification.

4 Conclusions

Here in this current work we demonstrated the use of a CW Nd:YAG laser to synthesize textured bioactive Ca–P coatings with 100 and 200 μm line spacing on Ti–6Al–4V substrate. XRD studies of the laser textured samples

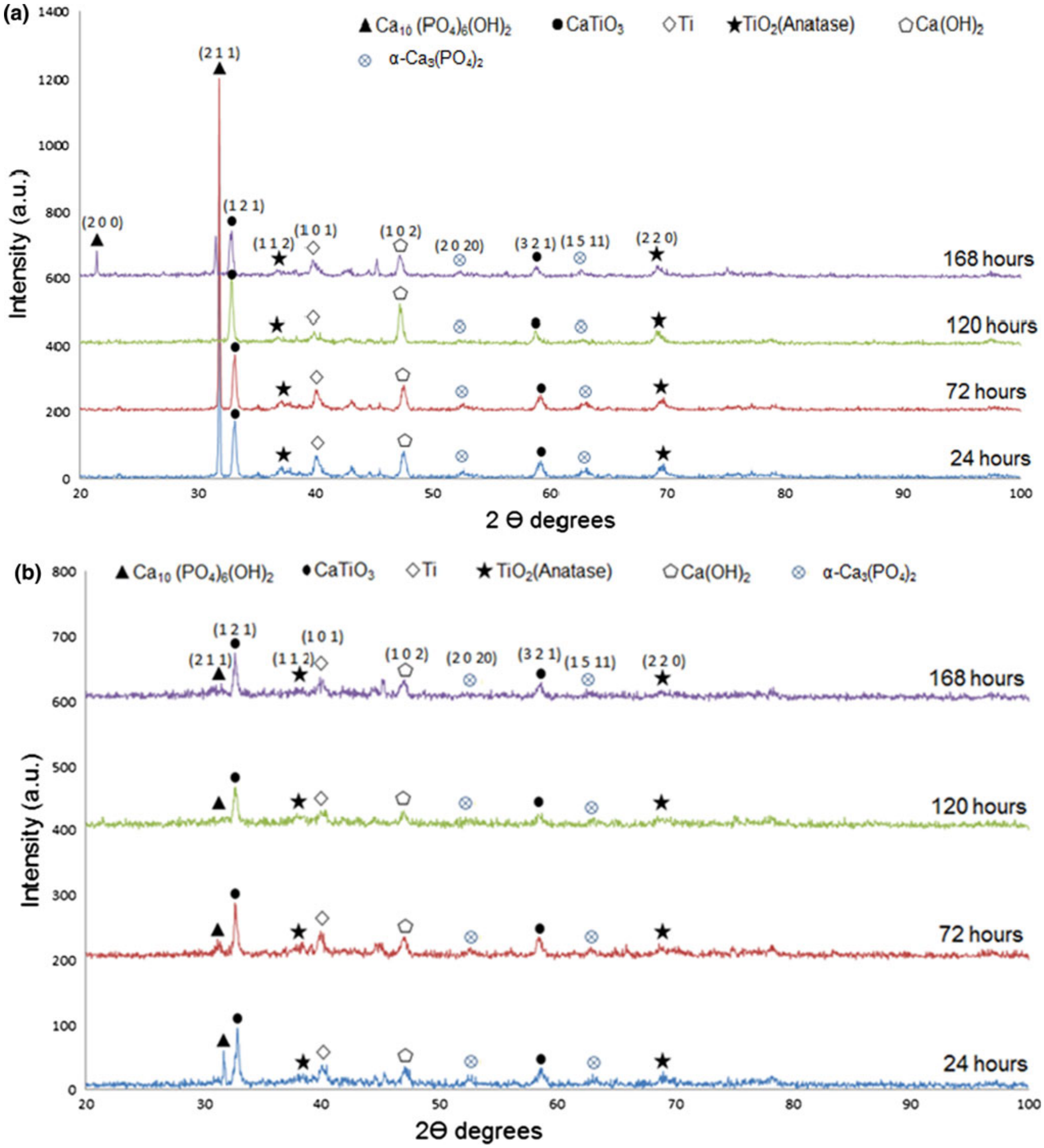

Fig. 7 XRD studies of **a** 137 J cm^{-2}, 100 μm line spaced and **b** 137 J cm^{-2}, 200 μm line spaced samples following immersion in SBF for different time periods

showed the presence of beneficial biocompatible phases such as $CaTiO_3$, TiO_2, α-TCP and $Ca(OH)_2$ within the coatings. Cross-sectional elemental mapping and composition line scans of the coatings indicated the presence of a thin layer Ca concentration (~10 μm) at the top and certain penetration of the P atoms (~100 μm) within the coating. Improved in vitro bioactivity of the textured coatings was proved by the formation of an apatite like

Fig. 8 FTIR spectra of laser processed samples: **a** 137 J cm^{-2}, 100 μm line spacing and **b** 137 J cm^{-2}, 200 μm line spacing and following immersion in SBF for different time periods

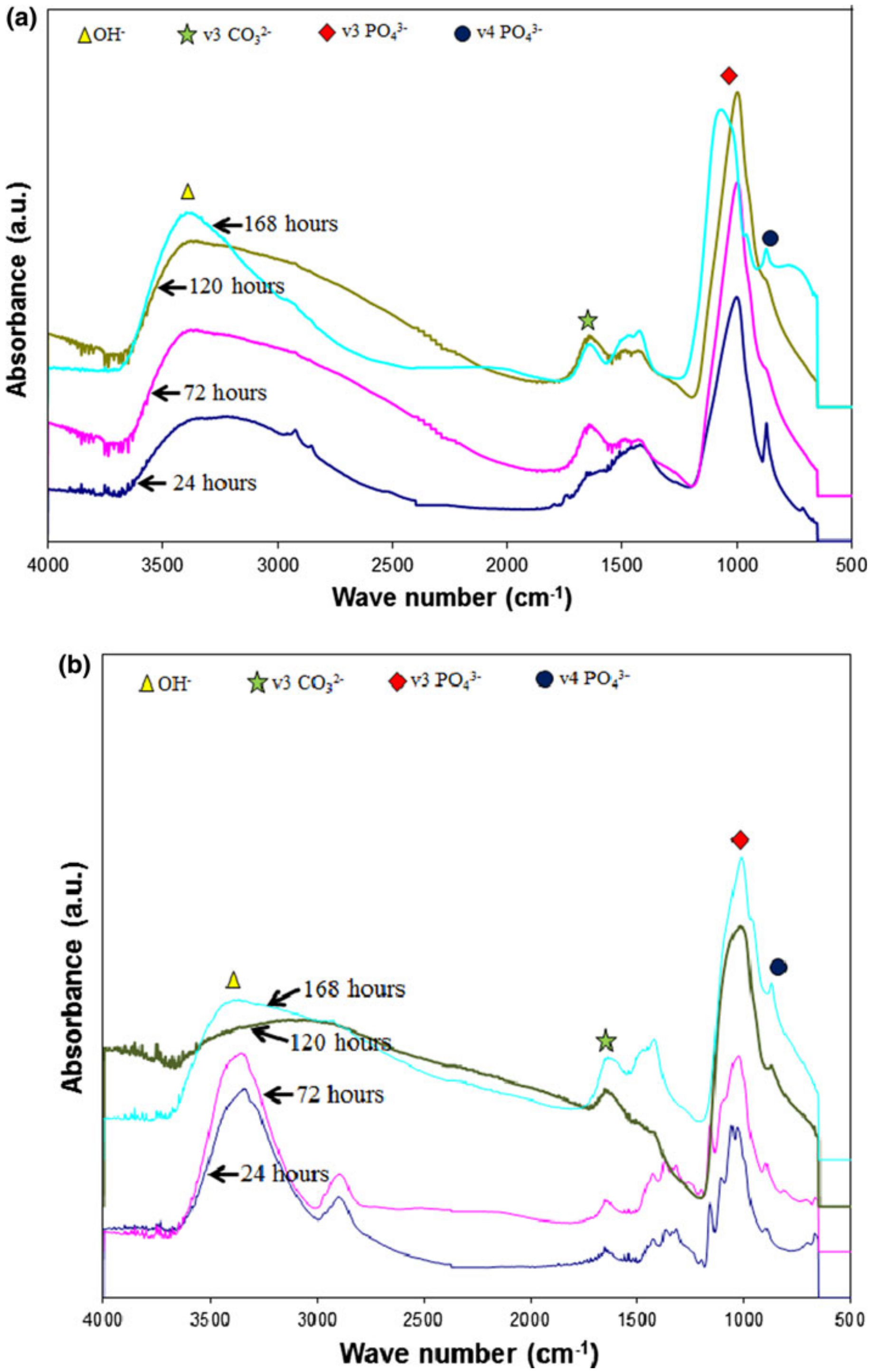

phase following immersion in SBF. XPS, XRD and FTIR analysis of the mineralized samples confirmed for the presence of apatite like phase on the surface of the sample. Improved in vitro biocompatibility on the textured coated samples as compared to the substrate Ti–6Al–4V substrate was characterized by the better cytoskeleton organization and spreading of the mouse MC3T3-E1 osteoblast-like cells. The above results therefore outlined the beneficial effects of laser surface modification to synthesize textured coatings with controlled surface features for load bearing implant applications.

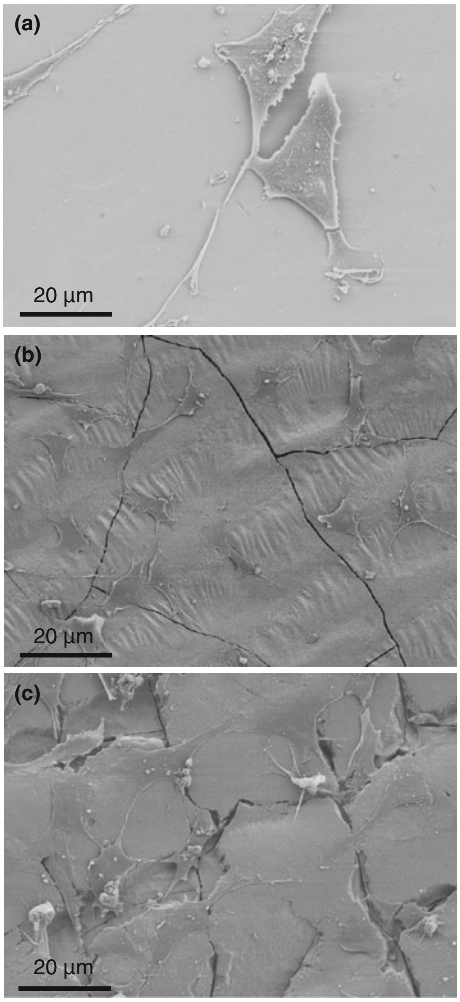

Fig. 9 Cell morphology of MC3T3-E1 osteoblast-like cells after culture for 1 day on **a** control (untreated Ti–6Al–4V), and samples processed at **b** 137 J cm^{-2}, 100 µm line spacing, and **c** 137 J cm^{-2}, 200 µm line spacing

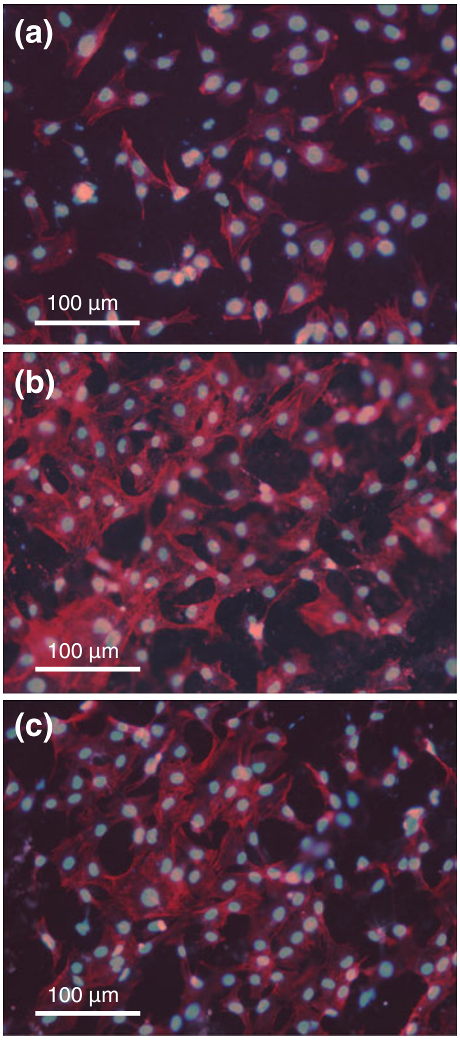

Fig. 10 Fluorescent micrographs for cytoskeleton assessment of adherent MC3T3-E1 osteoblast-like cells after culture for 1 day on **a** control (untreated Ti–6Al–4V substrate) and samples processed at **b** 137 J cm^{-2}, 100 µm line spacing and **c** 137 J cm^{-2}, 200 µm line spacing

References

1. Palson BØ, Bhatia SN. Tissue engineering. 1st ed. Prentice Hall: Pearson; 2004. P. 252–5.
2. Paital SR, Dahotre NB. Calcium phosphate coatings for bio-implant applications: materials, performance factors and methodologies. Mater Sci Eng R. 2009;66:1–70.
3. Ji H, Ponton CB, Marquis PM. Microstructural characterization of hydroxyapatite coating on titanium. J Mater Sci Mater Med. 1992;3:283–7.
4. Boyd AR, Meenan BJ, Leyland NS. Surface characterization of the evolving nature of radio frequency magnetron sputter deposited calcium phosphate thin films after exposure to physiological solution. Surface Coat Technol. 2006;200:6002–13.
5. Haddow DB, James PF, Van Noort R. Sol-gel derived calcium phosphate coatings for biomedical applications. J Sol–Gel Sci Technol. 1998;13:261–5.
6. Nelea V, Ristoscu C, Chiritescu C, Ghica C, Mihailescu IN, Pelletier H, Mille P, Cornet A. Pulsed laser deposition of hydroxyapatite thin films on Ti–5Al–2.5Fe substrates with and without buffer layers. Appl Surf Sci. 2000;168:127–31.
7. Shirkhanzadeh M. Bioactive calcium phosphate coatings prepared by electrodeposition. J Mater Sci Lett. 1991;10:1415–7.
8. Kitsugi T, Nakamura T, Oka M, Senaha Y, Goto T, Shibuya T. Bone-bonding behavior of plasma sprayed coatings of Bioglass^{R}, AW-glass ceramic, and tricalcium phosphate on titanium alloy. J Biomed Mater Res. 1996;30:261–9.
9. Wang BC, Lee TM, Chang E, Yang CY. The shear strength and failure mode of plasma-sprayed hydroxyapatite coating to bone: the effect of coating thickness. J Biomed Mater Res. 1993;27:1315–27.
10. Hench LL. Bioceramics: from concept to clinic. J Am Ceram Soc. 1991;74:1487–510.
11. Ratner BD, Hoffman AS, Schoen FJ, Lemons JE. Biomaterials science. 2nd ed. San Diego: Elsevier; 2004.
12. Paital SR, Balani K, Agarwal A, Dahotre NB. Fabrication and evaluation of a pulse laser-induced Ca–P coating on a Ti alloy for bioapplication. Biomed Mater. 2009;4:1–10.

13. Paital SR, Dahotre NB. Wettability and kinetics of hydroxyapatite precipitation on laser textured Ca–P bioceramic coating. Acta Biomater. 2009;5:2763–72.
14. Paital SR, Dahotre NB. Laser surface treatment for porous and textured Ca–P bio-ceramic coating on Ti–6Al–4V. Biomed Mater. 2007;2:274–81.
15. Dahotre NB, Paital SR, Samant AN, Daniel C. Wetting behaviour of laser synthetic surface microtextures on Ti–6Al–4V for bio-application. Philos Trans Roy Soc A. 2010;368:1863–89.
16. Yang Y, Paital SR, Dahotre NB. Effects of SiO_2 substitution on wettability of laser deposited Ca–P biocoating on Ti–6Al–4V. J Mater Sci Mater Med. 2010;21:2511–21.
17. Lusquiños F, Pou J, Arias JL, Boutinguiza M, León B, Pérez-Amor M, Driessens FCM, Merry JC, Gibson I, Best S, Bonfield W. Production of calcium phosphate coatings on Ti–6Al–4V obtained by Nd: yttrium–alluminium–garnet laser cladding. J Appl Phys. 2001;90:4231–6.
18. Lusquiños F, De Carlos A, Pou J, Arias JL, Boutinguiza M, León B, Pérez-Amor M, Driessens FCM, Hing K, Gibson I, Best S, Bonfield W. Calcium phosphate coatings obtained by Nd:YAG laser cladding: physicochemical and biologic properties. J Biomed Mater Res A. 2003;64:630–7.
19. Lusquiños F, Pou J, Boutinguiza M, Quintero F, Soto R, León B, Pérez-Amor M. Main characteristics of calcium phosphate coatings obtained by laser cladding. Appl Surf Sci. 2005;247:486–92.
20. De Carlos A, Lusquiños F, Pou J, León B, Pérez-Amor M, Driessens FCM, Hing K, Best S, Bonfield W. In vitro testing of Nd:YAG laser processed calcium phosphate coatings. J Mater Sci Mater Med. 2006;17:1153–60.
21. Wang DG, Chen CZ, Ma J, Zhang G. In situ synthesis of hydroxyapatite coating by laser cladding. Colloids Surf B. 66:155–62.
22. Weidong Z, Qibin L, Min Z, Xudong W. Biocompatibility of a functionally graded bioceramic coating made by wide-band laser cladding. J Biomed Mater Res A. 2008;87:429–33.
23. Stevens MM, George JH. Exploring and engineering the cell surface interface. Science. 2005;310:1135–8.
24. Kokubo T, Kushitani H, Sakka S, Kitsugi T, Yamamuro T. Solutions able to reproduce in vivo surface-structure changes in bioactive glass ceramic A-W. J Biomed Mater Res. 1990;24(6):721–34.
25. Kokubo T, Takadama H. How useful is SBF in predicting in vivo bone bioactivity? Biomaterials. 2006;27(15):2907–15.
26. Kasemo B. Biological surface science. Surf Sci. 2002;500:656–77.
27. Assender H, Bliznyuk V, Porfyrakis K. How surface topography relates to materials properties. Science. 2002;297:973–6.
28. Paital SR, Cao Z, He W, Dahotre NB. Wetting effects on in vitro bioactivity and in vitro biocompatibility of laser micro-textured Ca–P coating. Biofabrication. 2010;2:1–14.
29. Wei D, Zhou Y, Jia D, Wang Y. Structure of calcium titanate/titania bioceramic composite coatings on titanium alloy and apatite deposition on their surfaces in a simulated body fluids. Surf Coat Technol. 2007;201:8715–22.
30. Coreño J, Coreño O. Evaluation of calcium titanate as apatite growth promoter. J Biomed Mater Res. 2005;75A:478–84.
31. Kunze J, Müller L, Macak JM, Greil P, Schmuki P, Müller FA. Time-dependent growth of biomimetic apatite on anodic TiO_2 nanotubes. Electrochem Acta. 2008;53:6995–7003.